

In-Situ Optical Coherence Tomography (OCT) for the Time-Resolved Investigation of Crystallization Processes in Polymers

Peter Hierzenberger,[†] Elisabeth Leiss-Holzinger,[‡] Bettina Heise,^{§,||} David Stifter,[§] and Gerhard Eder*,[†]

[†]Institute of Polymer Science, Johannes Kepler University, Altenberger Straße 69, 4040 Linz, Austria

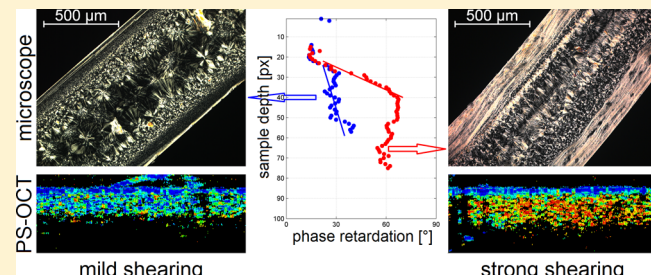
[‡]Research Center for Non-Destructive Testing, Altenberger Straße 69, 4040 Linz, Austria

[§]Christian Doppler Laboratory for Microscopic and Spectroscopic Material Characterization, Center for Surface and Nanoanalytics, Johannes Kepler University, Altenberger Straße 69, 4040 Linz, Austria

^{||}FLLL, Institute for Knowledge-based Mathematical Systems, Johannes Kepler University, Altenberger Straße 69, 4040 Linz, Austria

Supporting Information

ABSTRACT: By application of optical coherence tomography (OCT), an interferometric noncontact imaging technique, the crystallization of a supercooled poly(propylene) melt in a slit die is monitored. Both the quiescent and the sheared melt are investigated, with a focus on experiments where solidification and flow occur simultaneously. OCT is found to be an excellent tool for that purpose since the resultant structures are strongly scattering, which is a prerequisite for application of that method. The resulting images enable for the first time to directly monitor structure development throughout the whole experiment, including final cooling to room temperature. By rendering the setup polarization-sensitive, information on the birefringence of the pertinent structures is obtained.



1. INTRODUCTION

Optical coherence tomography (OCT) is a low-coherence interferometric imaging method which was developed in the 1990s prevalently in the area of biomedical diagnostics.¹ It generates depth scans of samples in a contact-free, non-destructive manner. Having become a standard method for ophthalmologic examinations,^{2,3} within the past decade also applications outside the medical field were found, as summarized in a recent review⁴ and with a special focus put on polymer science: in contrast to biological tissues, polymers usually do not contain water and therefore also light in the near-infrared (NIR) region, which otherwise would be absorbed, can be used. With an NIR light source at a central wavelength of 1550 nm, penetration depths in the millimeter range were obtained, qualifying OCT as a method suited for investigations on a processing scale.

In the current work, we investigate for the first time another specific application of OCT, namely the monitoring of polymer crystallization.⁵ It is well-known that, upon processing, polymers form various structures depending on the prevalent thermal conditions, pressure, and deformation.⁶ At the same time, this morphology directly influences the mechanical and optical properties of the resultant plastic part. Considerable research has therefore been dedicated to assessing the effect of processing parameters on the final properties.⁷ A number of methods are available, starting with the ex-situ analysis of microtome cuts, which is still a valuable tool for the characterization of solidified samples.⁵ However, it does not

directly give the situation in the melt. This can only be accomplished by in-situ methods, e.g. hot-stage microscopy, polarimetry,⁸ various scattering methods (light, neutron, and X-ray), rheo-optical techniques,⁹ or dilatometric measurements.^{10,11} With these methods, structure development can be monitored as a function of time, but usually they give only an integral or averaged measure of different processes occurring in the sample instead of depth-resolved information. An ingenious idea was presented by Fernandez-Ballester et al.,¹² who used a set of shear experiments observed via synchrotron X-ray scattering and optical retardance to calculate the incremental contribution of different shear rates and thus in fact obtained depth-resolved information. However, apart from the fact that considerable effort is necessary to perform a set of synchrotron measurements, like many of the previously mentioned methods also this one experiences limits if the effects become too complicated, namely with multiple scattering in consequence of long shearing times.

OCT, as presented in this paper, represents a major advance over these conventional methods in two respects: first, it delivers both depth- and time-resolved information in real time out of a single measurement, and second, it is not restricted by advanced structure development. In fact, it even works the better the more reflective structures have been formed. OCT

Received: November 17, 2013

Revised: February 26, 2014

Published: March 14, 2014



thus enables to extend shearing times to more realistic, industrial processing conditions, being unaffected by heavy shearing conditions.

To our knowledge, the present investigation represents the first time of flow-induced structure development being monitored *in situ* and in a depth-resolved way.

2. EXPERIMENTAL SECTION

Description of the Method. The principle of OCT is based on white light interferometry but uses broadband light sources in the near-infrared range (700–1600 nm).^{1–3} Most OCT systems employ a Michelson interferometer, where spatially coherent and temporally incoherent light emitted by a light source (LS) is split into a sample and a reference beam by a beam splitter (BS), as shown in Figure 1.

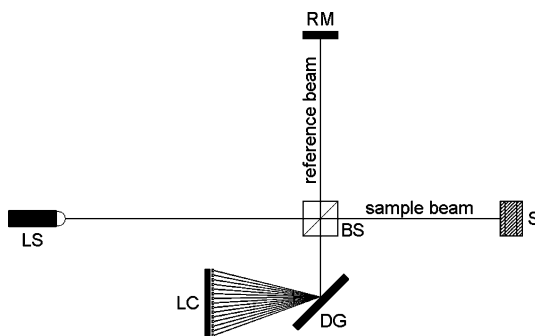


Figure 1. Setup for a Fourier-domain OCT (FD-OCT). Abbreviations: LS = light source, BS = beam splitter, RM = reference mirror, S = sample, DG = diffraction grating, and LC = line camera.

The reference beam is reflected by a mirror (RM), while the sample beam is focused into the sample and reflected by interfaces in the sample, physically spoken by inhomogeneities in the refractive index. Both reflected beams are then recombined at the beam splitter. The larger the difference in the refractive index, the more light is reflected. This gives rise to a measurable quantity, the reflectivity R , which is recorded as a function of the sample depth z .

The interferometric detection scheme of OCT provides high sensitivity and a high dynamic range, so that extremely small reflections of 10^{-10} can be accurately measured¹³ even in case of absorbing or scattering media.

Two different approaches can be distinguished, namely time-domain (TD-OCT) and Fourier domain (FD-OCT). The first one, TD-OCT, detects the recombined beams by a single photodetector. Only photons contribute to the signal which are reflected at a certain depth of the sample where the sample path length matches the reference path length. Depth scans are performed by mechanically moving the reference mirror. The second approach, FD-OCT, which is shown in Figure 1, analyzes the spectrum of the recombined beam in a spectrometer. A diffraction grating (DG) splits the beam into its spectral components, which are detected by a line camera (LC). By Fourier transform of the measured spectrum, an immediate complete depth-resolved reflectivity scan is obtained without the need for mechanical movement of the reference mirror.¹⁴ Though more expensive due to the camera, this method is superior in terms of speed and signal-to-noise ratio when compared to TD-OCT. Additionally, it enables rapid scanning at several adjacent positions, in order to create cross-sectional images. This is usually implemented by deflecting the sample beam to different positions on the sample via a small tilting mirror (galvo scanner).

An enhanced variant analyzes the polarization state of the reflected light, which renders the OCT polarization-sensitive (PS-OCT).¹⁵ A pertinent system has for the first time been described by Hee et al.;¹⁶ it uses quarter-wave plates to illuminate the sample with circularly polarized light, whereas the light exiting the reference arm is rendered linearly polarized in 45°. Combined with the FD approach, a

polarization-sensitive Fourier domain OCT (PS-FD-OCT) is obtained as shown in Figure 2.

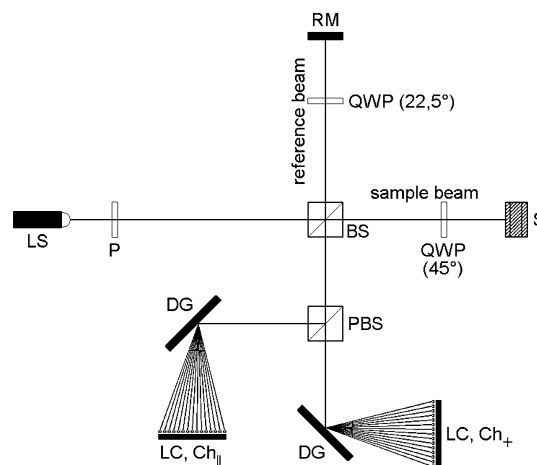


Figure 2. Extension of Figure 1 for polarization sensitivity (PS-FD-OCT) by adding additional components: P = polarizer, QWP = quarter-wave plate, PBS = polarizing beam splitter. The orientation of the quarter-wave plates is given in brackets. The outgoing signal is split in two orthogonally polarized components and recorded by two line cameras, corresponding to data channels Ch_{\parallel} and Ch_{\perp} (parallel respectively crossed to the polarizer P).

Birefringence in the sample causes an additional optical retardation Γ between the two orthogonal light components, calculated by the integral over the birefringence Δn experienced along the optical path until to a sample depth z :

$$\Gamma(z) = \int_0^z \Delta n(z') dz' \quad (1)$$

With the analyzed beam crossing the sample twice (before and after reflection), this optical retardation comes into effect twice. In general, the circular polarization of the sample beam is changed to elliptical. For detection, the signal is split by a polarizing beam splitter (PBS) in two orthogonally polarized components, corresponding to channels Ch_{\parallel} and Ch_{\perp} . The index refers to the polarizer P and gives the parallel respectively the crossed component. The reflectivity is then obtained by adding the squared signals of both channels:¹⁷

$$R(z) = Ch_{\parallel}(z)^2 + Ch_{\perp}(z)^2 \quad (2)$$

Forming the ratio of both channels gives rise to a second quantity, the phase retardation δ calculated by¹⁷

$$\delta(z) = \arctan \frac{Ch_{\perp}(z)}{Ch_{\parallel}(z)} \quad (3)$$

denoting the phase shift between the two orthogonal polarization components. The signals $Ch_{\perp}(z)$ and $Ch_{\parallel}(z)$ detected by the cameras are always positive. Therefore, the calculated phase retardation δ oscillates between 0° and 90° with increasing optical retardation Γ . The total phase shift can be calculated by unwrapping.¹⁸ For instance, one full oscillation from 0° to 90° and back to 0° corresponds to a total phase shift of 180°. Analogously, multiorder birefringence leading to phase shifts above 360° is detected by adding up the contributions of all full oscillations. Since birefringence is steadily increasing during the experiment, phase retardation equally has to grow and the direction is unique.

OCT provides a lateral resolution R_{lat} that is determined by the focusing of the laser spot size on the sample, i.e., by the numerical aperture of the optical system:

$$R_{\text{lat}} \sim 1/NA \sim \lambda \frac{f}{D} \quad (4)$$

with f as the focal length of a focusing lens and D the beam diameter. The axial (depth) resolution R_{ax} is independent of the lateral resolution and proportional to the square of the central wavelength λ_c but inversely proportional to the spectral bandwidth $\Delta\lambda$ of the light source:^{2,3}

$$R_{ax} = \ln 2 \frac{2 \lambda_c^2}{\pi \Delta\lambda} \quad (5)$$

Spectrally broader light sources are therefore of advantage. A smaller central wavelength λ_c is even more effective in improving the resolution but leads to stronger scattering and consequently reduces the penetration depth. Thus, when choosing between sources with the same bandwidth, the one with longer central wavelength permits deeper penetration on the cost of axial resolution. With current light sources, axial resolutions in the micrometer range can be reached.³

Apparatus. A self-developed polarization-sensitive Fourier domain OCT apparatus (PS-FD-OCT) is mounted on a shear system in order to directly observe crystallization *in situ* (Figure 3). For the light

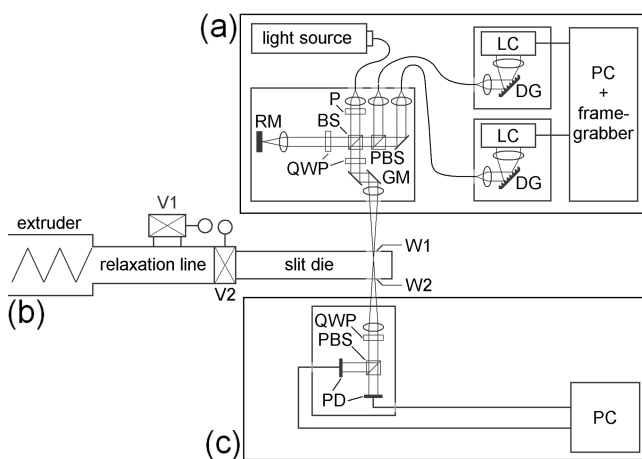


Figure 3. Top view of the experimental setup: (a) OCT unit: RM = reference mirror, QWP = quarter-wave plate, BS = beam splitter, P = polarizer, PBS = polarizing beam splitter, GM = galvo mirror, DG = diffraction grating, LC = line camera. (b) Shear unit: V1, V2 = valves, W1 = front window, W2 = rear window. (c) Transmission stage: QWP = quarter-wave plate, PBS = polarizing beam splitter, PD = photodiodes.

source, a superluminescence diode (Exalos) with a central wavelength of $\lambda_c = 1540$ nm and a spectral bandwidth of $\Delta\lambda = 55$ nm is used, operating in the near-infrared range and providing a satisfactory penetration depth of more than 1 mm.⁴ According to eq 5, the axial resolution is $19 \mu\text{m}$ in air. Assuming an average refractive index of $n \approx 1.5$ for polymer materials, the axial resolution obtained within such samples improves to $R_{ax} \approx 13 \mu\text{m}$. A galvo scanner enables fast adjacent depth scans along vertical lines, so that cross-sectional *in-situ* images in a plane perpendicular to the extrusion direction are generated. Spectral analysis is performed by diffraction gratings, from which the dispersed spectra are directed to CCD line cameras (InGaAs, Sensors Unlimited). The recorded spectra are numerically Fourier transformed to obtain the depth-resolved information. Our system is capable of recording four full cross sections (1000×512 pixels) per second for the *in-situ* measurements.

The shear unit consists of an extruder, a relaxation line, and a slit die (length 120 mm) of large aspect ratio (10 mm \times 1 mm cross section), as described by Liedauer et al.⁸ for short-term shearing experiments. By a special valve system (V1 and V2 in Figure 3), box-like pressure profiles can be applied for extrusion. At the end of the die, two windows (W1 and W2) are mounted through which the OCT sample beam is directed. Light that is reflected by the polymer sample goes back through the front window W1 and is analyzed in the OCT

system, generating a reflectivity and a phase retardation signal, both depth-resolved. The other portion of light is transmitted through the rear window W2 and is analyzed in analogy to former experiments with a polarized, monochromatic laser beam:¹⁹ a quarter-wave plate compensates for the optical retardation introduced by the sample quarter-wave plate, so that the light would be linearly polarized if no birefringence were found in the sample. Subsequently, the signal is decomposed into two orthogonally polarized components by a polarization-sensitive beam splitter and registered by photodiodes (InGaAs amplified detectors, Thorlabs). From the intensities registered at both diodes, the relative intensity of each component is calculated. With reference to the first polarizer of the OCT unit, one signal is assigned to the relative intensity at parallel polarizers $i_{||}$ and the other one to the relative intensity at crossed polarizers i_{\perp} . Both are correlated to the optical retardation by¹⁹

$$i_{\perp} = 1 - i_{||} = \sin^2 \frac{\pi \Gamma}{\lambda} \quad (6)$$

Provided that the optical retardation measured in transmission is entirely caused by the sample, i.e., there is no contribution from the windows, it has to be equal to the optical retardation measured in reflection at the backside of the sample. Therefore, this transmitted signal can directly be correlated to the phase retardation signal from OCT.

Material and Experimental Protocol. For the experiments presented in this paper, isotactic poly(propylene) (DM55pharm from Borealis, Linz/Austria) is used. The granules are melted in the extruder and the die is filled with hot melt at 200 °C. After a relaxation period of 15 min, the die is quenched with diethylene glycol to a temperature of 140 or 145 °C; at these temperatures, the material crystallizes only very slowly if left under quiescent conditions. After another 15 min for thermal equilibration, shearing is induced by resuming extrusion at a constant pressure of 175 or 200 bar for a defined period of time ranging from 0 to 200 s, and subsequent structure development is monitored by OCT and by the transmission signal. After 40 min of isothermal structure development, the die is cooled to room temperature and the sample is extracted. Microscopic analysis of microtome cuts as well as ex-situ OCT performed on the bare sample is used for verification of the obtained morphology.

During extrusion, a plug flow type of velocity profile develops, characterized by high shear rates close to the die walls and nearly zero shear rate in the central part of the sample, where flow velocity is highest (Figure 4a). Using a Cartesian coordinate system, there is one prominent axis x_1 , given by the extrusion direction. For optical characterization, this prominent direction defines a uniaxial system. The other axes are x_2 , which is the direction of the velocity gradient,

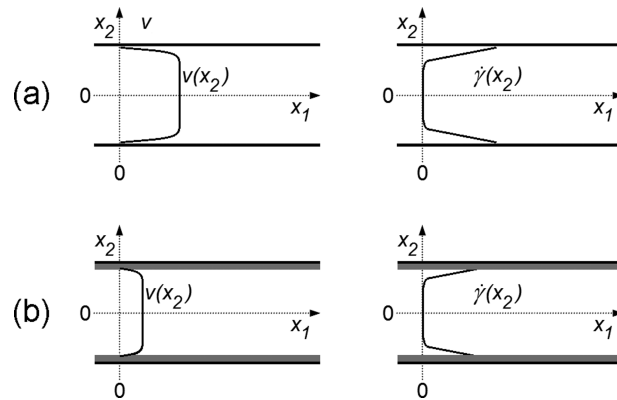


Figure 4. Flow velocity v and shear rate $\dot{\gamma}$ profile in a slit die, with coordinate axes x_1 and x_2 . The third coordinate axis x_3 is directed normally to the paper plane. (a) Plug flow type profile without solidification; (b) cutoff profile after narrowing of the channel due to solidification at the die walls.

and x_3 , the neutral direction, which is perpendicular to the small side walls of the die.

Shearing leads to the alignment of molecules in the x_1 direction and therefore enhances crystallization; especially for poly(propylene), it is well-known that different morphologies develop:⁷ with very high shear rates, so-called shish-kebabs are found, which are highly birefringent. With the shear rate profile decreasing and leveling off toward zero, also this morphology changes to a spherulitic one, as would be found under quiescent conditions. In between the fully spherulitic core and the highly oriented layer, a transition region is found which is usually called the fine-grained layer due to its appearance under the optical microscope. Typical morphologies as observed on microtome sections under the polarization microscope are depicted in Figure 5. They have been cut in the x_1-x_2 plane, so that this figure is analogous to Figure 4.

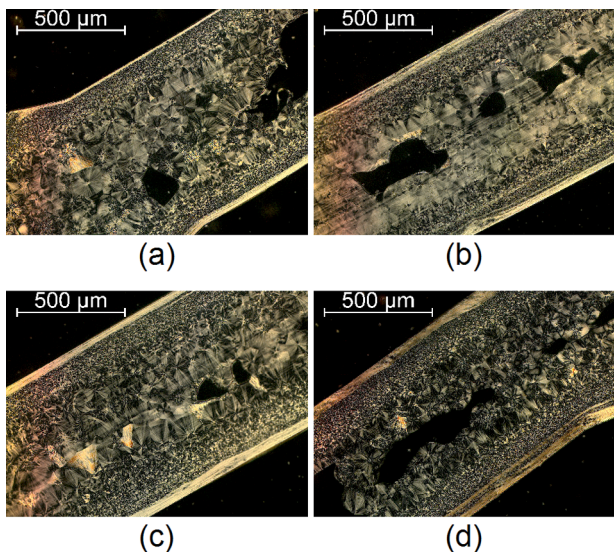


Figure 5. Morphologies of samples produced at 145 °C and 175 bar, cut in the x_1-x_2 plane. Holes in the microtome cuts result from the final stage of crystallization due to the constraints built by the solidified surroundings. Shearing times: (a) 50, (b) 100, (c) 150, and (d) 200 s.

Naturally, as soon as some of the material has solidified on the die walls in form of one of these morphologies, the flow cross section decreases. However, by extruding at constant pressure, the shear rate profile in the still flowing part does not change. Only the velocity profile is cut off, i.e., its shape remains constant, but the boundary condition $v = 0$ is shifted with the solidification front toward the central part of the die (Figure 4b), leading to a reduced overall velocity.

For OCT measurements, the laser beam is aligned to the x_2 axis, which therefore coincides with the sample depth, and is circularly polarized in the x_1-x_3 plane. Lateral scanning is performed in this experimental configuration along the x_3 direction for in-situ OCT, leading to images oriented in the x_2-x_3 plane. For ex-situ OCT, the lateral scanning direction can freely be chosen either in the extrusion direction x_1 or perpendicularly as in in-situ OCT. In both cases, the ellipticity of the reflected beam represents the corresponding anisotropy of the refractive index $n_1 - n_3 = \Delta n_{13}$. In contrast, microtome cuts are prepared in the x_1-x_2 plane, and accordingly the contrast of the transmission polarization microscopy arises from Δn_{12} . However, due to the radial symmetry of the individual crystalline structures in the x_2-x_3 plane, both results can directly be compared and correlated to each other.

3. RESULTS

Reflectivity Measurements. Flow-induced structure development can effectively be observed in a depth-resolved way in OCT reflectivity images. Figure 6 shows a sequence of in-situ

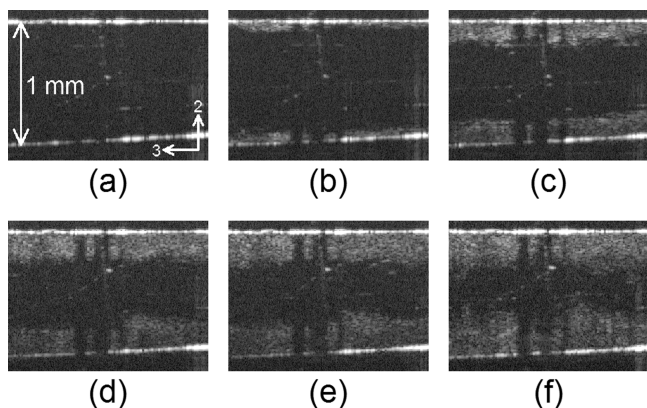


Figure 6. In-situ OCT reflectivity images taken at different times t : a = 0, b = 50, c = 148, d = 300, e = 600, and f = 1460 s after the beginning of shearing. Temperature 140 °C, extrusion pressure during shearing 200 bar, shearing time 150 s. A wall shear rate of 25 s⁻¹ was calculated.

images taken at different times (0, 50, 148, 300, 600, and 1460 s) after the beginning of shearing. The temperature was 140 °C and the extrusion pressure 200 bar, leading to a wall shear rate of 25 s⁻¹. With the shearing time being 150 s, the first three images are taken still during the shearing period. The two limiting bright lines in each image represent the interfaces between the windows and the polymer, which is enclosed in between them. The extrusion direction x_1 is perpendicular to the image plane, the velocity gradient x_2 vertical in the image plane, and the neutral direction x_3 horizontal in the image plane.

The growth of structures is clearly visible already in the second image, taken 50 s after the beginning of shearing. Obviously, in the beginning crystallization does not proceed homogeneously along the neutral direction. Only after the end of shearing, a more or less straight front is formed (cf. images d–f). The structures that develop are not necessarily permanent, especially as long as flow persists: it is a regular phenomenon that parts adhere to the wall for a while, but then are ripped off by flow again. Flow must thus be attributed both a constructive as well as a destructive effect on structure development.

With milder shearing conditions or no shearing at all, also other morphologies can be observed. As an example, individual spherulites are shown in Figure 7a. They have been obtained at a temperature of 140 °C, an extrusion pressure of 175 bar, and a rather short shearing time of only 5 s. Not all of these spherulites are in a fixed position yet; especially those in the center of the sample are still moving. With such flowing

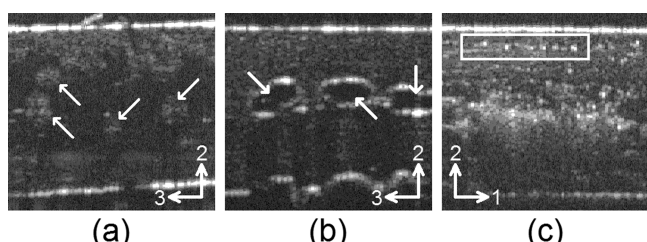


Figure 7. Features directly visible in OCT reflectivity images: (a) spherulites, (b) voids, (c) linearly shaped structures. (a) and (b) were acquired in situ in a direction perpendicular to the extrusion direction; (c) was recorded ex situ in extrusion direction.

particles the original model assumption of a flowing continuum is no longer valid, and also nonlinear flow patterns are observed. Spherulites represent also rewarding objects for related OCT techniques, as recently demonstrated for the example of polarization-sensitive full-field optical coherence microscopy (PS-FF-OCM).²⁰

Figure 7b shows voids, another feature visible in reflectivity. The refractive index within the voids ($n = 1$) shortens the optical path length, so that the rear window appears shifted upward below them. This image is a good example for the advances obtained with OCT: For measurements in transmission, voids represent strongly backscattering obstacles and destroy the measurement signal, so that analysis of such structures could not be performed at all.

A further interesting feature is visible in the ex-situ OCT image presented in Figure 7c: in contrast to the typical in-situ images, where flow is perpendicular to the paper plane, this image was scanned in the extrusion direction, which is now horizontal. Linear structures are clearly visible, prevalently close to the sample surface, which are most probably related to a shish-kebab structure or any other threadlike morphology generated by high shear rates.

Polarization-Sensitive OCT. So far several phenomena have been shown for the first time to be directly observable in reflectivity images. Furthermore, our equipment is also polarization-sensitive. In the resulting retardation images, the phase retardation as calculated by eq 3 is mapped for all points of sufficient reflectivity. For the sample in the melt state, there are no reflective points at all, and birefringence becomes visible only at the rear window, which represents a reflective interface throughout the whole experiment.

Figure 8 shows the development of phase retardation as a function of time, as detected at the rear window. For that

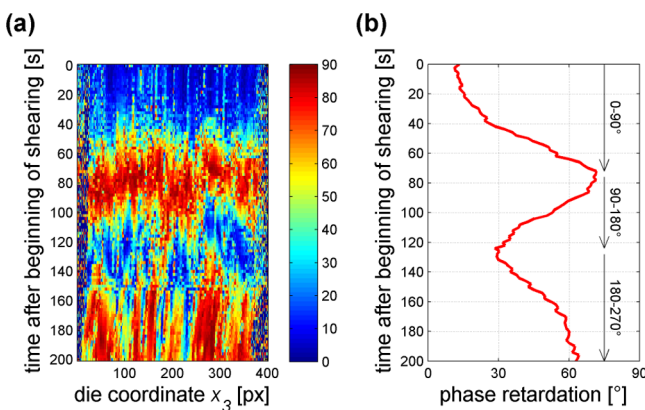


Figure 8. (a) Phase retardation as a function of time, as detected at the rear window. For the graph, the respective pixels have been extracted from PS-OCT retardation images and plotted as rows with time as the vertical coordinate. 400 pixel in the x_3 direction correspond to approximately 0.7 mm. (b) Phase retardation profile as a function of time, calculated by the mean values of each row in (a). By summing up the phase retardation of each half-cycle, the total phase shift is obtained, as marked by arrows. The experiment is the same as in Figure 6.

purpose, the pixels forming the rear window have been extracted from PS-OCT retardation images. Each horizontal line corresponds to a different monitoring time, starting with shearing (top line) and ending 200 s after the beginning of shearing (bottom line) with intervals of 2 s. The experiment is

the same as shown in Figure 6. Ideally, retardation should change synchronously over the whole image width, which coincides with the neutral direction. However, the experiment shows some deviations; they correspond to the nonuniformity of the crystallization process in Figure 6. Still, three half-cycles in phase retardation change from blue (0°) over red (90°) back to blue and once again to red are clearly visible, corresponding to a total change of 270° . For later times (not shown in the figure), depolarization occurs, leading to some mixture of retardation values in a broader range. For determination of absolute values, the mean value of each line is taken. By this procedure, the time evolution of the total phase retardation can be calculated, which is shown in Figure 8b.

An analogous change of retardation is found in the retardation images, but now as a function of sample depth. Figure 9 shows an image and its phase retardation profile, again

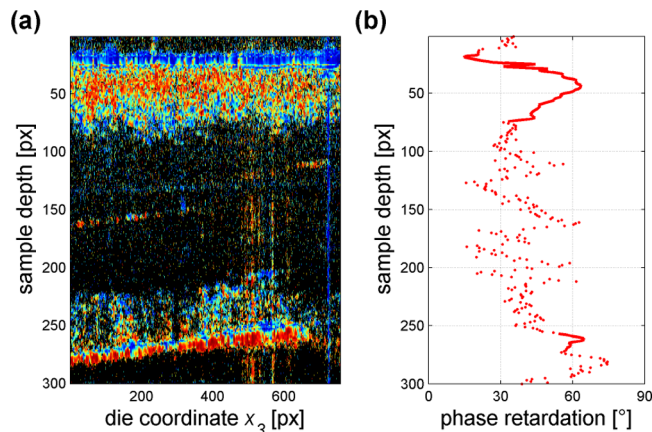


Figure 9. (a) Phase retardation as a function of sample depth, as directly visible in retardation images. Points with insignificant retardation values are left black. (b) Phase retardation profile as a function of sample depth, derived from the mean values of all significant points of each row in (a). For the central, nonreflective part only arbitrary values are obtained (dotted line). Temperature 140 °C, extrusion pressure during shearing 200 bar, shearing time 200 s, recorded 216 s after the beginning of shearing.

obtained by forming the average of all reflective points per line. Phase retardation is clearly increased by the solidified structures, which therefore must be birefringent. The area in the center of the sample is nonreflective, so the profile does not show any relevant information here, but for the rear window the phenomenon can equally be observed. By using phase unwrapping and calculating the derivative of the unwrapped retardation over depth, even quantitative access to the birefringence depth profile is gained.^{18,21}

With this ability to directly reveal information on the birefringence of structures, PS-OCT enables further conclusions on the morphology generated. As outlined above, morphology strongly depends on the prevalent shearing conditions. This is shown in Figure 10, where a weakly sheared sample (140 °C, 200 bar, 25 s) is directly compared to a heavily sheared sample (140 °C, 200 bar, 150 s). The different morphology is clearly visible in the microtome cuts produced afterward from the solidified samples, exhibiting only a very thin highly oriented layer, but a broad fine-grained layer with mild shearing (Figure 10a). Quite the opposite is seen in the strongly sheared sample (Figure 10c), which shows only a highly birefringent layer directly neighboring the spherulitic

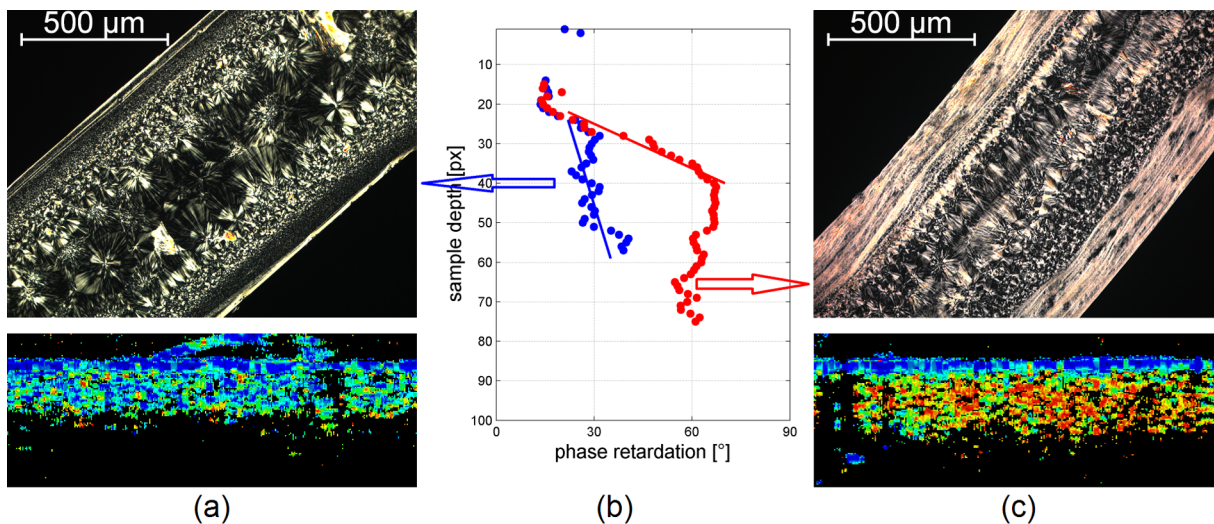


Figure 10. Comparison of (a) a weakly sheared sample ($140\text{ }^{\circ}\text{C}$, 200 bar, 25 s) with (c) a heavily sheared sample ($140\text{ }^{\circ}\text{C}$, 200 bar, 150 s). For both measurements, a microtome cut and the front window region of the OCT retardation image are shown. In (b) the respective phase retardation profiles are given, exhibiting different degrees of birefringence (with lines as guide to the eye, indicating the initial slopes).

core morphology. In the PS-OCT images analogous information is found: phase retardation changes from blue (at the front window) to cyan or green in the weakly sheared sample, corresponding to $\delta = 45^{\circ}$ – 60° , whereas in the strongly sheared sample it changes to red ($\delta = 90^{\circ}$) and then even back to green already shortly after the front window. The phase retardation profile (Figure 10b) emphasizes the difference. From the slopes of the lines indicated in Figure 10b, a mean value for the birefringence can be calculated²¹ with $\Delta n \approx 4 \times 10^{-4}$ and 3×10^{-3} for the fine-grained and the highly oriented structure, respectively. Consequently, PS-OCT enables differentiation between the two morphologies on the basis of their birefringence even *in situ* during the formation of such structures.

Correlation with Transmission Signals. In addition to the measurement by PS-OCT, optical retardation was also monitored by analysis of the transmitted light. This information is in principle equal to the one obtained at the rear window (cf. Figure 8). However, while PS-OCT returns the phase retardation δ according to eq 3, transmission measurements give the optical retardation Γ via the relative intensity at crossed polarizers i_{\perp} and at parallel polarizers i_{\parallel} according to eq 6. By inserting the extreme values of $\delta = 0^{\circ}$ or 90° the correlation of both methods becomes more obvious: for $\delta = 0^{\circ}$, i_{\perp} is 0 and i_{\parallel} is 1. For $\delta = 90^{\circ}$, both i_{\perp} and i_{\parallel} reach a value of 0.5; i.e., they show a crossover.

Consequently, Figure 11 shows for validation a comparison of the mean value of the phase retardation, as obtained from the rear window, with the relative intensity signals registered in the transmission stage. Measurements at $145\text{ }^{\circ}\text{C}$ are given. Those with the longer shearing times (150 and 200 s) exhibit clear maxima in phase retardation, which correspond to $\delta = 90^{\circ}$, a value which is however not fully reached due to depolarization and averaging over lateral inhomogeneities. The maxima coincide perfectly with the first crossover in the relative intensities, as indicated by vertical lines. Measurements with shorter shearing times (50 and 100 s) do not reach a phase retardation approaching 90° , correspondingly avoiding a crossover in the relative intensities, too. With these results, PS-OCT is proven to substitute also the transmission

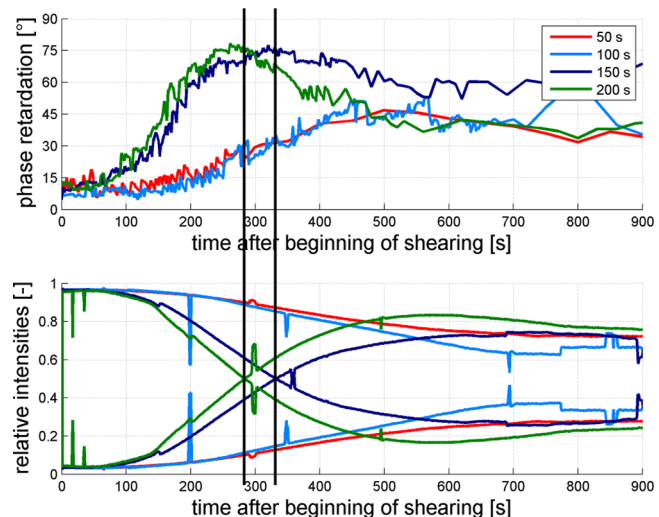


Figure 11. Mean value of phase retardation δ from PS-OCT (top) and relative intensities in transmission measurements (bottom), both versus time with 0 = beginning of shearing. For the two longest shearing times, in phase retardation pronounced maxima are found which coincide with a crossover in the relative intensities, as indicated by the two vertical lines. For the shorter shearing times, due to the formation of more depolarizing structures neither a clear maximum in phase retardation nor a crossover in the intensities is found. Temperature $145\text{ }^{\circ}\text{C}$, extrusion pressure during shearing 175 bar, shearing times as indicated in the legend.

measurements, besides delivering in addition depth resolved information as shown in Figure 10.

In a qualitative comparison, the retardation and relative intensities in Figure 11 run synchronously as long as shearing persists; then they split. The first maximum in the phase retardation and crossover in the relative intensities is the earlier, the longer the shearing time; i.e. more birefringent structures are formed, being also at the same time of less depolarizing nature, as indicated by the more pronounced maxima in both types of curves.

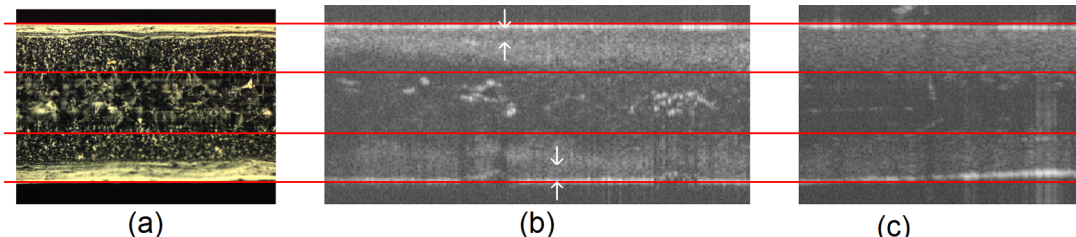


Figure 12. Comparison of (a) a microtome cut with (b) ex-situ and (c) in-situ OCT reflectivity images. The structure detected in OCT corresponds to both the highly oriented and the fine-grained layer, with a slight difference in the degree of reflectivity being detectable (marked by arrows).

4. DISCUSSION AND CONCLUSION

The results presented above demonstrate for the first time that OCT is ideally suited for monitoring in situ the growth of structures due to shearing or even in the quiescent melt. However, knowing there are different morphologies dependent on the local shear rate, the method seems for the chosen wavelength region indifferent with respect to the type of morphology. In fact, OCT is sensitive in the reflectivity images on both the highly birefringent *and* the fine-grained layer, although slight differences in the degree of reflectivity can be detected in the ex-situ images, as shown in Figure 12: here, a microtome cut under the polarization microscope is compared with an ex-situ and an in-situ image of the same sample. The in-situ image has been taken at the end of the isothermal crystallization period, so that shear-induced structure development is basically finished and the image can be compared with the two others. All images have been scaled to equal size; the red lines indicate the border of the structures visible in OCT.

By PS-OCT, samples exhibiting exclusively either the fine-grained or the highly oriented layer can clearly be differentiated, as has been demonstrated by Figure 10, where the difference in the change of phase retardation is clearly visible. Also, the agreement with measurements in transmission is evident (Figure 11). For differentiation of the layers within the same sample, the depth resolution of the current setup is too low and values derived directly from PS-OCT suffer considerable scattering. This is also a drawback of the reflectivity images shown, which becomes evident especially on comparison with the microscope. However, depth resolution depends strongly on the light source, as specified by eq 5; it might be crucially improved by measurements at a shorter wavelength. Development of advanced light sources, especially with broader bandwidth, should therefore be able to further increase the potential of OCT.

ASSOCIATED CONTENT

Supporting Information

A movie demonstrating in-situ monitoring of polymer crystallization directly in the slit die, with the following parameters: temperature 140 °C, extrusion pressure during shearing 200 bar, shearing time 150 s. This material is available free of charge via the Internet at <http://pubs.acs.org>.

AUTHOR INFORMATION

Corresponding Author

*Tel +43 732 2468 8756, e-mail gerhard.eder@jku.at (G.E.).

Notes

The authors declare no competing financial interest.

ACKNOWLEDGMENTS

The present work has been carried out in the course of the project P19751-N20 of the Austrian Science Fund FWF. Further financial support from the Austrian Federal Ministry of Economy, Family and Youth, the National Foundation for Research, Technology and Development, by the European Regional Development Fund (EFRE) and the federal state Upper Austria is acknowledged. We are grateful to C. K. Hitzenberger and his team at the Medical University of Vienna for support in the setup of the PS-OCT system. The first author thanks Josef F. Pühringer for his comments and thorough discussion during preparation of this paper.

REFERENCES

- (1) Huang, D.; Swanson, E. A.; Lin, C. P.; Schuman, J. S.; Stinson, W. G.; Chang, W.; Hee, M. R.; Flotte, T.; Gregory, K.; Puliafito, C. A.; Fujimoto, J. G. *Science* **1991**, *254*, 1178–1181.
- (2) *Handbook of Optical Coherence Tomography*; Bouma, B. E., Tearney, G. J., Eds.; Marcel Dekker: New York, 2002.
- (3) *Optical Coherence Tomography, Technology and Applications*; Drexler, W., Fujimoto, J. G., Eds.; Springer: Berlin, 2008.
- (4) Stifter, D. *Appl. Phys. B: Lasers Opt* **2007**, *88*, 337–357.
- (5) Eder, G.; Janeschitz-Kriegl, H. *Mater. Sci. Technol.* **1997**, *18*, 269–342.
- (6) Kornfield, J. A.; Kumaraswamy, G.; Issaian, A. M. *Ind. Eng. Chem. Res.* **2002**, *41*, 6383–6392.
- (7) Janeschitz-Kriegl, H. *Crystallization Modalities in Polymer Melt Processing*; Springer: New York, 2010.
- (8) Liedauer, S.; Eder, G.; Janeschitz-Kriegl, H.; Jerschow, P.; Geymayer, W.; Ingolic, E. *Int. Polym. Proc.* **1993**, *VIII*, 236–244.
- (9) Baert, J.; van Puyvelde, P.; Langouche, F. *Macromolecules* **2006**, *39*, 9215–9222.
- (10) van Erp, T. B.; Balzano, L.; Spoelstra, A. B.; Govaert, L. E.; Peters, G. W. M. *Polymer* **2012**, *53*, 5896–5908.
- (11) Rudolph, N. M.; Osswald, T. A.; Ehrenstein, G. W. *Int. Polym. Proc.* **2011**, *XXXVI*, 239–248.
- (12) Fernandez-Ballester, L.; Thurman, D. W.; Kornfield, J. A. *J. Rheol.* **2009**, *53*, 1229–1254.
- (13) Minoshima, K.; Kowalevicz, A. M.; Hartl, I.; Ippen, E. P.; Fujimoto, J. G. *Opt. Lett.* **2001**, *26*, 1516–1518.
- (14) Fercher, A. F.; Hitzenberger, C. K.; Kamp, G.; El-Zaiat, S. Y. *Opt. Commun.* **1995**, *117*, 43–48.
- (15) Stifter, D.; Burgholzer, P.; Höglinder, O.; Götzinger, E.; Hitzenberger, C. K. *Appl. Phys. A: Mater. Sci. Process.* **2003**, *76*, 947–951.
- (16) Hee, M. R.; Huang, D.; Swanson, E. A.; Fujimoto, J. G. *J. Opt. Soc. Am. B* **1992**, *9*, 903–908.
- (17) Hitzenberger, C. K.; Götzinger, E.; Sticker, M.; Pircher, M.; Fercher, A. F. *Opt. Expr.* **2001**, *9*, 780–790.
- (18) Stifter, D.; Leiss-Holzinger, E.; Major, Z.; Baumann, B.; Pircher, M.; Götzinger, E.; Hitzenberger, C. K.; Heise, B. *Opt. Expr.* **2010**, *18*, 25712–25725.
- (19) Jerschow, P.; Janeschitz-Kriegl, H. *Rheol. Acta* **1996**, *35*, 127–133.

- (20) Heise, B.; Schausberger, S.; Stifter, D. In *Optical Coherence Tomography*; Kawasaki, M., Ed.; InTech: Rijeka, Croatia, 2013; Chapter 8, p 139; DOI: 10.5772/56293.
- (21) Wiesauer, K.; Sanchis Dufau, A. D.; Götzinger, E.; Pircher, M.; Hitzenberger, C. K.; Stifter, D. *Acta Mater.* **2005**, *53*, 2785–2791.